

PREDICTING FUTURE SPACE NEAR-IR GRISM SURVEYS USING THE WFC3 INFRARED SPECTROSCOPIC PARALLELS SURVEY

JAMES W. COLBERT¹, HARRY TEPLITZ², HAKIM ATEK^{3,1}, ANDREW BUNKER⁴, MARC RAFELSKI¹, NATHANIEL ROSS⁵, CLAUDIA SCARLATA⁶, ALEJANDRO BEDREGAL⁶, ALBERTO DOMINGUEZ⁷, ALAN DRESSLER⁸, ALAINA HENRY⁹, MATT MALKAN⁵, CRYSTAL L. MARTIN¹⁰, DAN MASTERS^{7,8}, PATRICK MCCARTHY⁸, BRIAN SIANA⁷*Draft version May 8, 2013*

ABSTRACT

We present near-infrared emission line counts and luminosity functions from the *HST* WFC3 Infrared Spectroscopic Parallels (WISP) program for 29 fields observed using both the G102 and G141 grism. Altogether we identify 1048 emission line galaxies with observed equivalent widths greater than 40 Å, 467 of which have multiple detected emission lines. We use simulations to correct for significant (>20%) incompleteness introduced in part by the non-dithered, non-rotated nature of the grism parallels. The WISP survey is sensitive to fainter flux levels ($3\text{--}5 \times 10^{-17}$ ergs s⁻¹ cm⁻²) than the future space near-infrared grism missions aimed at baryonic acoustic oscillation cosmology ($1\text{--}4 \times 10^{-16}$ ergs s⁻¹ cm⁻²), allowing us to probe the fainter emission line galaxies that the shallower future surveys may miss. Cumulative number counts of $0.7 < z < 1.5$ galaxies are in rough agreement with the corrected count predictions of H α emitters from Geach et al. (2010), reaching 10,000 deg⁻² above an H α flux of 2×10^{-16} ergs s⁻¹ cm⁻². H α -emitting galaxies with comparable [OIII] flux are roughly 5 times less common than galaxies with just H α emission at those flux levels. Galaxies with low H α /[OIII] ratios are very rare at the brighter fluxes that future near-infrared grism surveys will probe; our survey finds no galaxies with H α /[OIII] < 0.95 that have H α flux greater than 3×10^{-16} ergs s⁻¹ cm⁻². Our H α luminosity function contains a slightly higher number density of faint line emitters than the NICMOS near-infrared grism surveys, likely a result of the smaller equivalent widths to which the WISP survey is sensitive. We also find that our high redshift ($z=0.9\text{--}1.5$) counts are slightly higher (factors of 1.3–2) than the high redshift ($z=1.47$) narrow band H α survey of HiZELS (Sobral et al. 2012), although our lower redshift luminosity function ($z=0.3\text{--}0.9$) is consistent with their $z=0.84$ result. The evolution in the [OIII] luminosity function from $z=0.7\text{--}2.3$ is almost entirely in the L_{*} parameter, which steadily increases with redshift over that range.

Subject headings: galaxies: evolution, galaxies: high-redshift, infrared: galaxies

1. INTRODUCTION

The majority of star formation, supermassive black hole accretion, and galaxy assembly in the universe likely occurred over the epoch of $z=0.7\text{--}2$ (e.g., McLure et al. 2006, Pérez-González et al. 2008, van Dokkum et al. 2010, Magnelli et al. 2011). A careful census of the spatial distribution of galaxies in this redshift range is critical for measuring the large-scale clustering of galaxies that results from baryonic acoustic oscillations (BAO),

which will enable us to probe the expansion history of the universe and address the equation state of dark energy (Eisenstein & Hu 1998, Cole et al. 2005, Eisenstein et al. 2005, Weinberg et al. 2012). Large near-infrared spectroscopic surveys are required to study this redshift regime, as the most luminous nebular emission lines move out of the optical at these redshifts.

Ground-based searches for emission lines from faint high-redshift galaxies are severely impacted by the bright near-IR airglow, which effectively eliminates the possibility of slitless grism spectroscopy. Most near-infrared ground spectroscopy is done a single object at a time, requiring some form of pre-selection that generally biases against discovery of the highest equivalent width sources. In the near future, multi-object near-infrared spectrographs on the world's largest telescopes (i.e. MOSFIRE, FLAMINGOS-2, MOIRCS, EMIR, KMOS, etc.) will allow for the study of a much greater number of galaxies, but even then they will be subject to the atmospheric transmission windows and an inability to discover the emission line objects with the most extreme equivalent widths.

An alternative method to spectroscopy for identifying large numbers of $z>0.7$ emission line galaxies are wide-field narrow band searches targeting the transmission windows in our atmosphere, e.g. HiZELS (Geach et al. 2008, Sobral et al. 2009, Sobral et al. 2012) and

¹ Spitzer Science Center, California Institute of Technology, Pasadena, CA 91125

² Infrared Processing and Analysis Center, Caltech, Pasadena, CA 91125, USA

³ Laboratoire d'astrophysique, École Polytechnique Fédérale de Lausanne, Observatoire de Sauverny, 1290 Versoix, Switzerland

⁴ Department of Physics, University of Oxford, Denys Wilkinson Building, Keble Road, Oxford OX1 3RH, UK

⁵ Department of Physics and Astronomy, University of California, Los Angeles, CA, USA

⁶ Minnesota Institute for Astrophysics, University of Minnesota, Minneapolis, MN 55455, USA

⁷ Department of Physics and Astronomy, University of California Riverside, Riverside, CA 92521, USA

⁸ Observatories of the Carnegie Institution for Science, Pasadena, CA 91101, USA

⁹ Astrophysics Science Division, Goddard Space Flight Center, Code 665, Greenbelt, MD 20771

¹⁰ Department of Physics, University of California, Santa Barbara, CA 93106, USA

CANDELS-COSMOS (Lee et al. 2012). These surveys have the advantage of very high sensitivity to emission lines ($\sim 1 \times 10^{-17}$ ergs s $^{-1}$), but suffer from an inability to map outside their narrow redshift ranges, making them unfeasible for BAO studies. In addition there is the danger of significant contamination from emission lines at different redshifts, a well known issue from high redshift Ly α emission line searches (Martin et al. 2008, Henry et al. 2012). For instance, the typical H α /[OIII] 5007 Å ratio decreases with redshift (Ly et al. 2007, van der Wel et al. 2011, Domínguez et al. 2013). A carefully constructed experiment, with multiple photometric bands along with additional narrow bands targeting another expected line at the same redshift, can increase the narrow band reliability (e.g., Lee et al. 2012, Sobral et al. 2012), although surveys dependent on continuum detections will still miss the lowest mass galaxies.

Of course the best way to avoid the limitations of the atmosphere is to observe in space. Two future space missions, ESA’s *Euclid* (Laureijs et al. 2012, Laureijs et al. 2011) and NASA’s *WFIRST* (Green et al. 2012, Dressler et al. 2012), both utilize large area, near-infrared grism surveys to investigate BAO, galaxy evolution, and star formation history. In addition to identifying the redshift of galaxies, near-infrared spectroscopy also allows access to the wealth of stellar evolution diagnostic features available in the optical: H α , one of the most reliable indicators of star formation rate, the Balmer decrement, to determine extinction, as well as multiple metallicity indicators. These emission line surveys will cover thousands of square degrees of continuous redshift space, unbiased by the underlying continuum luminosity of the galaxy. However, these will not be the first near-infrared grism observations done from space, as the *Hubble Space Telescope* has had two instruments with near-infrared grisms.

The Near IR Camera and Multi-Object Spectrometer (NICMOS, Thompson & Schneider 1998) G141 grism pure-parallel program (McCarthy et al. 1999, Yan et al. 1999, Shim et al. 2009), surveyed ~ 170 arcmin 2 , identifying 113 emitters, and measuring the H α -luminosity function from $0.7 < z < 1.9$. The NICMOS data had a tiny (< 1 arcmin 2) field of view, low spectral resolution ($R \sim 100$), and relatively poor detector sensitivity. The Wide Field Camera 3 (WFC3; MacKenty et al. 2010) instrument is an improvement in all three areas, providing a 20-fold survey efficiency gain for the presently on-going WFC3 Infrared Spectroscopic Parallels program (WISP; Atek et al. 2010, 2011). While much smaller in area, the WISP survey is much deeper than the future space near-infrared grism surveys. There is presently no better laboratory for predicting what these future missions can expect.

In this paper we discuss a sample of the WISP emission line objects identified from $0.85 - 1.65 \mu\text{m}$. We discuss the survey, details of the emission line extraction, completeness corrections, and estimates of redshift accuracy. We then present the H α and [OIII] line-emitter number counts, H α /[OIII] ratios, and luminosity functions. Finally, we present our final summary and conclusions. We assume an $\Omega_M=0.3$, $\Omega_\Lambda=0.7$ universe with $H_0=70$ km s $^{-1}$ Mpc $^{-1}$. All magnitudes are in the AB system.

2. WISP SURVEY

The WISP survey (PI=Malkan, GO-11696, GO-12283, GO-12568, & GO-12902) consists of HST WFC3 (Kimble et al. 2008) grism observations in uncorrelated high-latitude fields obtained in parallel mode while prime observations are being obtained with the Cosmic Origins Spectrograph (COS; Osterman et al. 2011) or the Space Telescope Imager and Spectrograph (STIS; Woodgate et al. 1998). The parallel data include both grism spectroscopy and associated near-IR and optical imaging. Depending on the length of the parallel opportunity, the WISP survey either acquires spectroscopy with just the G141 ($1.2-1.7 \mu\text{m}$, $R \sim 130$) grism or, in the case of longer opportunities, a combination of G141 and the G102 ($0.8-1.2 \mu\text{m}$, $R \sim 210$) grism with roughly 2-3 times more integration time spent on the higher resolution G102 grism. At a plate scale of 0.13 arcsec pixel $^{-1}$, the total field of view for each observation is $123'' \times 136''$. We note that one can only achieve the full grism wavelength resolution for compact sources, as any spatial extension of the object will also broaden the features within the spectrum. See Atek et al. (2010) for further discussion of the program.

For this paper we present data from 29 separate fields where we have both G102 and G141 grism spectroscopy, covering a total of 135 arcmin 2 over 159 orbits. These fields, along with their integration times, are presented in Table 1. While other large G141 grism surveys have been approved by HST (e.g., 3D-HST and AGHAST; Brammer et al. 2012, Weiner 2012), no other program comes close to surveying the area that WISP does with such an extended spectral coverage ($0.85-1.65 \mu\text{m}$).

The inclusion of the G102 grism doubles the wavelength and redshift range surveyed. More importantly, it provides both critical checks of the assumed redshift and multiple line ratios that can not be obtained using G141 alone. [OIII] and H α only fall together on the G141 grism over a very narrow redshift range ($z=1.3-1.55$), otherwise in the vast majority of cases G141-only observations only discover single emission lines. [OIII] lines of comparable or greater strength than H α are common (Hu et al. 2009, Atek et al. 2010, Domínguez et al. 2013), making a catastrophic misidentification likely. With both G102 and G141, WISP is sensitive to H α , [OIII], H β , and [OII] over a wide range of redshifts, and for $z=1.3-1.55$, we are sensitive to all those lines simultaneously.

3. EMISSION LINE EXTRACTION

All the data were processed with the WFC3 pipeline CALWF3 (ver. 2.1) to correct for bias, dark, flat-field, and gain variations. Then, the slitless extraction package aXe 2.0 (Kümmel et al. 2009) is used for the spectral extraction. A complete description of the data reduction steps is presented in Atek et al. 2010.

To locate and identify all the emission lines within our spectra we applied an automatic line finding algorithm. We first fit a three-segment cubic spline to the continuum of our one-dimensional aXe-extracted spectra, using outlier rejection to avoid fitting any emission lines. We then subtract the estimated continuum from the spectrum and divide the continuum-subtracted spectrum by the aXe estimate of the flux uncertainties for each pixel. This produces a signal-to-noise spectrum. We look for groupings of three or more contiguous pixels with an excess above the continuum with signal-to-noise in each

TABLE 1
SUMMARY OF WISP FIELD OBSERVATIONS

Field	RA [HMS]	Dec [DMS]	G102 [sec]	F110W [sec]	G141 [sec]	F160W [sec]
Par17	02:13:38.11	+12:54:59.3	3409	534	3409	559 ^a
Par55	12:20:54.68	-02:04:46.0	6415	909	2809	484 ^a
Par62	13:01:16.20	-00:00:20.2	4712	734	2006	396
Par64	14:37:29.04	-01:49:49.5	5918	1112	2306	456
Par68	23:33:33.04	+39:21:20.5	7721	1215	3009	534
Par69	15:24:07.75	+09:54:53.9	5721	1087	2309	431
Par73	14:05:12.86	+46:59:19.9	6118	1034	2509	456
Par74	09:10:48.14	+10:17:20.3	5918	1065	2306	431
Par76	13:27:22.17	+44:30:39.3	5515	887	2006	406
Par78	23:28 34.06	+05:10:28.3	5318	887	2106	406
Par79	01:10:08.96	-02:25:16.2	7521	1187	2809	534
Par81	01:10:09.12	-02:22:17.1	7521	1187	2809	534
Par87	09:46:46.39	+47:14:58.2	4915	912	1906	406
Par94	22:05:26.66	-00:17:48.5	9024	1624	3309	534
Par96	02:09:24.40	-04:43:41.6	28081	4295	11430	1765
Par97	01:10:06.30	-02:23:44.7	5515	859	2109	406
Par114	10:40:58.09	+06:07:31.0	7221	1137	2909	456
Par115	11:18:55.08	+02:17:09.6	5215	912	2106	381
Par120	13:56:51.50	+17:02:33.9	4512	837	1806	381
Par124	18:32:28.28	+53:44:50.9	4618	759	1906	406
Par129	11:02:18.72	+20:52:07.8	4712	762	2206	456
Par131	10:48:22.94	+13:03:50.5	13039	2171	5215	884
Par132	11:26:19.80	-01:43:22.1	4315	634	1806	356
Par135	11:22:24.01	+57:50:58.9	4712	862	1906	406
Par136	12:26:28.84	+05:23:02.9	18857	3036	7318	1137
Par143	14:02:22.01	+09:45:51.7	10133	1568	4012	759
Par146	02:12:27.60	-07:32:20.7	4212	887	1706	381
Par147	23:58:19.51	-10:15:04.6	5418	962	2106	406
Par167	01:41:24.18	+13:37:34.1	4315	659	1806	356

^a Used F140W as the direct image used for identifying counterparts in the G141 grism.

pixel greater than $\sqrt{3}$. For an unresolved object, the emission lines can be as narrow as two pixels and so we adopt a more-stringent two-pixel criterion of two contiguous pixels with a signal-to-noise ratio of greater than $\sqrt{5}$ in each. To validate this method of finding candidate emission lines, we compared several samples of emission lines found automatically to those found by an intensive, spectra by spectra, visual inspection and found the automated method did not miss any significant fraction of lines (<5%).

The parallel nature of the WISP observations presents several challenges to emission line extraction. Foremost is the lack of dithering, which greatly complicates the mitigation of cosmic rays, hot or warm pixels, and other artifacts. As a practical matter, this means that the automated line identification process has a very high contamination rate from false and/or spurious sources.

To address the false detections we require the visual inspection of every candidate emission line by two team members, done independently and without consultation. After this initial inspection, we compare the emission line lists from the two reviewers and send each reviewer back a list of discrepancies, allowing them to make a second, more careful examination of any emission lines for which there is a disagreement. This exercise provides a good final agreement for most emission lines, but we find that for roughly 5% of the emission lines, consensus can not be reached. These uncertain lines are removed from the final sample, but are accounted for in our completeness corrections (see Section 3.1).

The visual inspection consists of examining both the extracted one dimensional and the original two dimensional spectra, as well as the continuum fits and measure-

ments of signal-to-noise. There are only four conditions for which we exclude a candidate line:

1) If the line is clearly an artifact, either a cosmic ray, a zero order image from a nearby bright source, a diffraction spike, ghost, or some other artifact clearly not associated with the spectrum in question.

2) If the continuum fit under the location of the emission line is highly inaccurate, artificially increasing the significance of the emission line. Many of the spectra contain breaks, both real and caused by nearby contamination from overlapping sources, which often lead to continuum errors of this sort.

3) If the local noise variations are larger than the flux uncertainties used by the automated line identification software, measuring lines at a higher significance than local noise conditions actually warranted. While the WFC3 detector and grism are fairly uniform and well-behaved, we find variations across the detector and locations where what appear to be non-Poissonian sources of noise exist. In these cases the automated recovery pipeline was likely to find every noise peak and call it a source.

4) If the contamination from nearby overlapping spectra is so great that we can not determine what source is producing the emission line. However, in most cases even severe overlapping source contamination can be untangled. We use multiple lines spread across the G102 and G141 grisms (only the real source produces the correct wavelength ratios in those cases), small pixel offsets from source center, and discrepancies between the size of the object and the spatial extent of the emission line as evidence for assigning the confused emission line to its proper source. Only if the source remains ambiguous

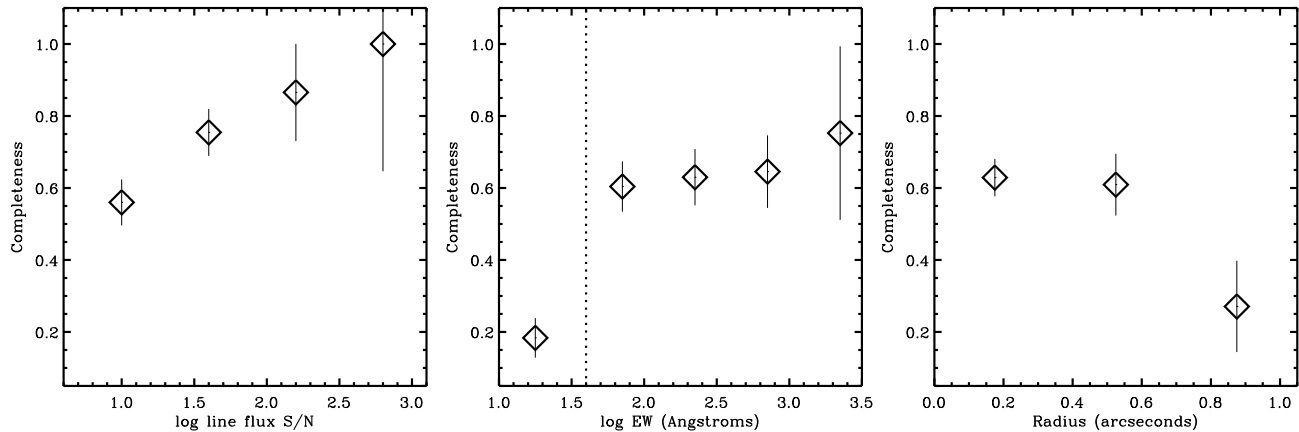


FIG. 1.— Completeness of extracted emission lines as a function of: *left*) line flux signal-to-noise, *middle*) equivalent width, and *right*) radius in arcseconds. The dotted line in the middle equivalent width plot represents the chosen equivalent width cut.

after all analysis is it excluded from the final sample.

Single emission lines are assumed to be $H\alpha$, except in the few rare circumstances where the single line is clearly resolved into the $[OIII]$ 5007+4959 Å doublet. Our simulations indicate that this is a good assumption and does not result in more than 6% of our $H\alpha$ lines being misidentified as $[OIII]$ (see Section 3.3 below). However, this assumption does have a large effect on the recovery of high redshift ($z > 1.5$) $[OIII]$ lines, requiring some additional completeness corrections for those emission lines (see Section 3.1.1).

In total, we extracted 1960 emission lines from the 29 fields down to a typical flux limit of $3\text{--}5 \times 10^{-17}$ ergs s^{-1} cm^{-2} . For an emission line galaxy to be included in our final analysis we also require an observed equivalent width greater than 40 Å ($\log EW = 1.6$; see Section 3.1 below) and a signal-to-noise greater than 5 for at least one of the detected emission lines, creating a final sample size of 1048 galaxies. Of these, 467 have multiple detected emission lines, including weaker $[OII]$, $H\beta$, and SII . For our final sample of emission line galaxies, we detect $H\alpha$ in 996 galaxies and $[OIII]$ in 280 galaxies. The overlap where we found both $H\alpha$ and $[OIII]$ in the same galaxy is 228.

3.1. Completeness Corrections

Virtually all surveys suffer incompleteness from objects lost as the strength of their signals approaches the level of the noise. A slitless grism survey, like WISP, also suffers significant incompleteness due to confusion from nearby bright sources. In addition to those two fundamental sources of incompleteness, emission lines can also be lost as part of the extraction methodology. These sorts of failures include objects missed by the automatic line finding routine, objects removed due to redshift confusion, and objects incorrectly rejected by visual inspection. In order to derive final completeness corrections to account for all the forms of incompleteness that effect the grism data, we must simulate the entire line extraction process from beginning to end.

We start with the generation of a set of emission line galaxy models, covering the full range of redshifts ($z=0.3\text{--}2$), brightnesses (19-26 F110W mag), spatial ex-

tent ($0.2\text{--}1''$ radius), equivalent widths (20-2000 Å) and line fluxes ($10^{-17} - 10^{-15}$ ergs s^{-1} cm^{-2}) found in our WISP data set of emission line galaxies. We then place each model galaxy randomly into one of our actual pairs of WISP G102 and G141 grism images using the aXeSIM software (Kümmel et al. 2007), before extracting it using the same methodology and pipeline as used for extracting all the real emission line galaxies. This means that first we identify the lines using the automated software and then two separate team members visually examine each spectrum to ensure it contains a real emission line. During the visual inspection we mix 15 model galaxies along with another 15 randomly chosen galaxies, such that the reviewer could not assume that each spectrum must contain a visible emission line. Overall we insert 923 model galaxies (74 fields each with typically 10-15 model galaxies) and, including the random galaxies, extract twice that number.

We find that the primary determinants of completeness for the emission line galaxy sample are the observed equivalent width (EW) and the line flux of the emission line. In practice, the latter translates to the signal-to-noise of the emission line flux measurement, as the background noise varied from field to field by a factor of 4. We also find completeness had some dependency on the radius (defined as the major and minor axis averaged in quadrature) of the source galaxy, but that this is of secondary importance due to relatively small number of large ($> 0.75''$) radius galaxies in the observed sample, approximately 0.5%. In Figure 1, we plot completeness as a function of these three parameters (line flux S/N, EW, and size), where each bin is a combination of recovery rates for the model galaxies. We weight all the model galaxy recovery rates for each single parameter by the frequency in which galaxies with the other two parameters appear in our full sample of actual emission line galaxies. For instance, if the full sample has twice as many small EW objects as large EW objects, model galaxies with small EWs will be given twice the weight when deriving completeness for S/N or size.

One immediate result from this simulation is that the recovery rate drops rapidly from 60% to $< 20\%$ as the observed EW (Å) of the emission line becomes less than

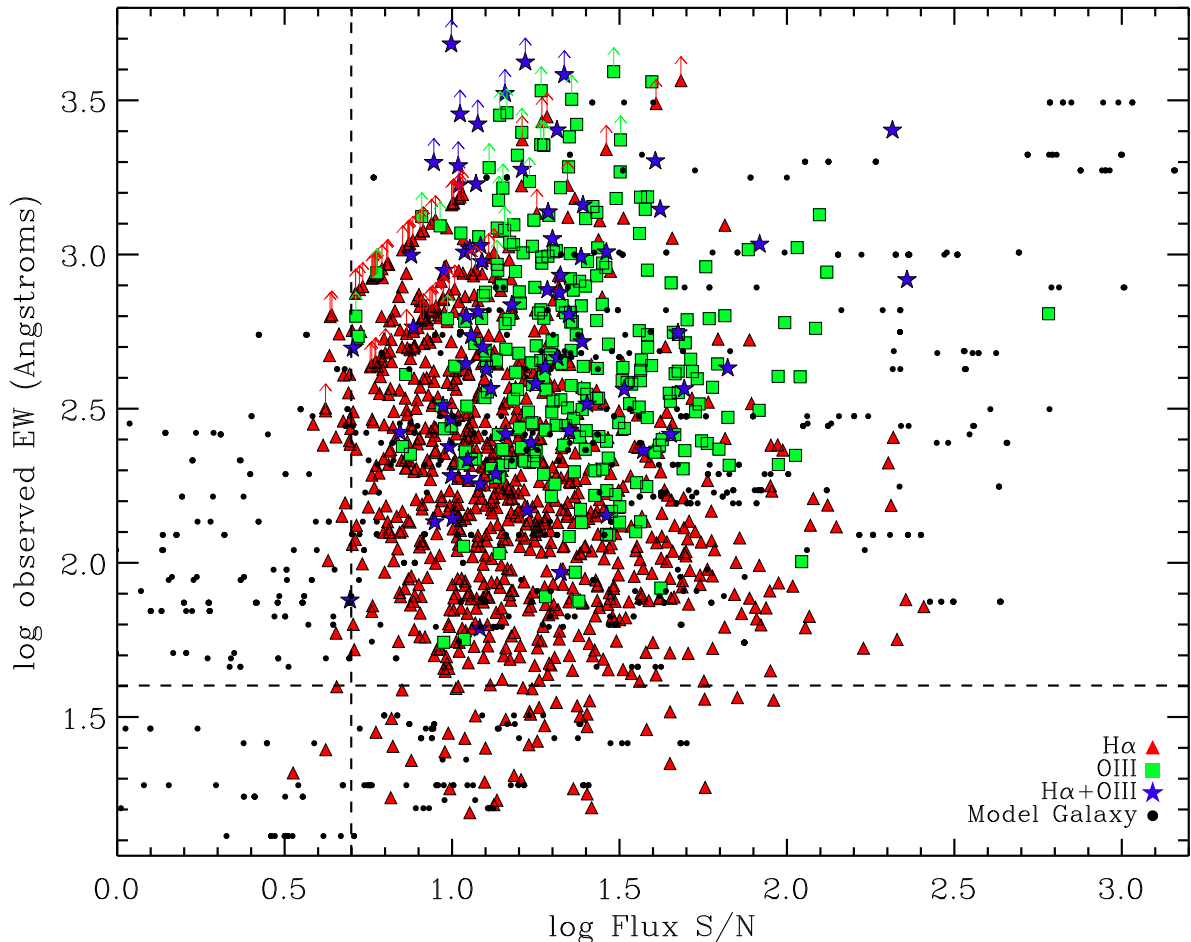


FIG. 2.— Plot of emission line flux signal-to-noise versus equivalent width for all the identified WISP emission lines. Red triangles are objects with $H\alpha$ emission lines, green squares are objects with $[OIII]$ emission, and blue stars are objects where both lines are detected. Where both $H\alpha$ and $[OIII]$ are detected, the parameters plotted are sums (EW) or quadratic sums (S/N) of the two lines together. Overplotted as solid black circles are the model emission line galaxies used for our completeness simulations. The dashed lines are the limits in flux and EW applied to our sample. Emission lines that lie beyond those limits have been excluded from the final analysis.

40 Å ($\log EW = 1.6$; see Figure 1). In the rest frame of our $z \sim 1$ galaxies, this EW limit corresponds to 20 Å, roughly two thirds that of the average $H\alpha$ EW for spiral galaxies in the Local Volume (Lee et al. 2007). In the interest of not introducing extremely large (> 5) and uncertain completeness corrections to the number counts, we apply a cut of $EW > 40$ Å to all of our analysis. After combining this EW cut with our requirement that all detected emission lines have a signal-to-noise > 5 , the total number of model galaxies is 553. Of those model galaxies, we recovered 380, yielding an approximate recovery rate of 69%. We note that for this combination of equivalent width and signal-to-noise, there are effectively no galaxies fainter than 25 magnitudes (as measured at F110W-band, although the simulated galaxies are flat in F_ν) in the final sample we use for our analysis.

In Figure 2, we present emission line EW as a function of signal-to-noise for both observed and model emission-line galaxies. One can see that the model galaxies span the same parameter range as the real galaxies, extending farther to brighter lines with large EWs and fainter lines with smaller EWs in order to test how our sample

completeness acts at these extremes. One complication is that over a significant portion of the redshift range ($z=0.7-1.5$), there are actually two strong emission lines, $[OIII]$ and $H\alpha$. In some cases $[OIII]$ is the more powerful line, particularly as we go to fainter line fluxes (see Section 4.2 below). We therefore used model templates both where $H\alpha$ is more powerful and ones where $[OIII]$ is the stronger emission line ($H\alpha/[OIII] = 0.75 - 4.3$).

One would expect a source with multiple lines to have a higher completeness than a single line source with the same line flux and EW. Therefore to determine the likelihood of identification, we measure the combined signal-to-noise of both lines, add them quadratically, and use that total signal-to-noise for calculating our completeness. For the combined EW we use a simple sum of the two emission lines. We plot these combined values of signal-to-noise and EW as blue stars in Figure 2, along with the single line cases of $H\alpha$ (red triangles) and $[OIII]$ (green squares). In most cases one line is clearly stronger, so the final signal-to-noise used for the completeness correction can usually be approximated as the signal-to-noise of just the brightest emission line. We do

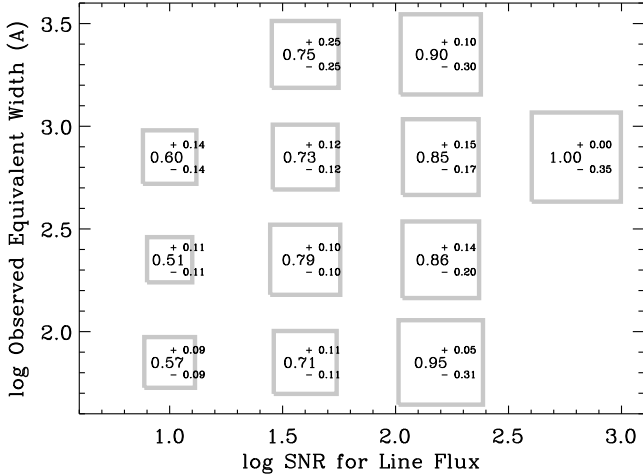


FIG. 3.— Diagram of completeness as a function of both line flux signal-to-noise and equivalent width. Each box represents one of the two parameter bins used, with the measured completeness ratio number inside it, including its error. The larger the square box, the smaller the completeness corrections that were applied for those emission line galaxies.

not use the other, weaker emission lines ([OII], SII, H β , etc.) for determining completeness, as these lines are never alone and their relative fluxes are almost always small compared to H α and [OIII].

We find that for even the highest signal-to-noise lines ($S/N > 100$), we reach only 90-95% completeness. The main reason for this is contamination, either from overlapping spectra or large, bright objects in the direct images used to identify the galaxy counterparts. Either the line is lost under an extremely bright spectrum (most fields have 3-5 moderately bright $H < 19$ objects), the object lies in a complicated region where we are unable to determine which of the nearby, overlapping objects to associate with the emission line, or the contamination from overlapping sources has caused the automatic line finder to fail, i.e., SExtractor fails to find the source or the continuum fit fails badly. Altogether contamination from nearby sources explains about 75% of line extraction failures. Most nearby source contamination issues would be resolved if data could be taken at two or more roll angles, such that the spectra do not overlap, but that is not an option for parallel programs. Another reason a strong line will fall out of our sample is if the two emission line reviewers can not come to consensus on the redshift of the object (10% of the bright extraction failures), which most commonly occurs where it is unclear whether the line is H α or [OIII]. For instance, when a source is spatially extended the grism wavelength resolution is effectively lowered, making it difficult to distinguish between the [OIII] doublet and a single emission line. This sort of confusion almost never occurs in G102 ($R \sim 210$), suggesting that data taken with a higher spectral resolution would largely solve this problem as well. The remaining $\sim 15\%$ of bright emission line failures are mostly miscellaneous extraction errors by the visual line inspectors.

In Figure 3, we plot the final completeness corrections used for all of our analysis, derived as a function of both the equivalent width and the signal-to-noise of the line

flux. While the object size also has an effect on whether an emission line galaxy will be recovered, we found that accounting for galaxy size has little effect on the overall completeness corrections, as the largest galaxies make up only a tiny percentage of the sample, $< 2\%$, even after accounting for their higher incompleteness. Or to put it another way, galaxy size is not very important to the overall completeness correction, because size completeness corrections grow larger as the actual number of galaxies is decreasing, unlike EW or line flux, where the number of objects tends to grow just as their completeness corrections are significantly increasing. A three parameter completeness correction is also not practical for the required double visual inspection of each suspected emission line. Each added parameter increases the human workload geometrically. Instead, for each bin of EW and line flux signal-to-noise, we weight the input model galaxies by the frequency that each galaxy size appears in our observed sample list of emission line galaxies.

3.1.1. [OIII] Completeness

Generally we found that the completeness corrections we derived for H α can also be applied to [OIII] emission lines. While [OIII] is a doublet with a distinctive line profile that one might expect could be more easily distinguished from artifacts and noise, for low signal-to-noise and small EWs where the incompleteness becomes increasingly important, [OIII] becomes indistinguishable from a single emission line.

This assumption that H α and [OIII] completeness can be treated the same breaks down for [OIII] at redshifts of $z > 1.5$. This is a result of the attribution of all single line emitters to H α . Below $z = 1.5$, H α remains in the wavelength range that is detectable by the WFC3 grisms and in the vast majority of cases if we detect an [OIII] emission line, the H α emission line will be detectable as well. This is because even down to our faintest emission line detections, the H α /[OIII] ratio is usually greater than 1 and rarely less than 0.4 (see Section 4.2). Above $z = 1.5$, the H α emission line is redshifted out of our detectable wavelength range, so we lose the ability to confirm [OIII] with the usually brighter H α line. If the [OIII] line is bright enough we can still identify it from its doublet line profile, but the faint [OIII] lines will all be identified as lower redshift H α lines by default.

While this misidentification of high- z [OIII] produces only a small contamination of H α (see Section 3.3), our simulations show we lose nearly 50% of our high- z [OIII] emission lines because of our inability to resolve the doublet. More specifically, the fainter the emission lines the larger the incompleteness. We have therefore added an additional completeness correction to our $z > 1.5$ [OIII] emission lines of 2.0 for $0.6 < \log S/N < 1.2$ and 1.6 for $1.2 < \log S/N < 1.8$. Higher signal-to-noise [OIII] emission lines require no additional correction.

3.2. Redshift Accuracy

Using the simulations we can also get an estimate of the redshift accuracy which is possible with grism spectroscopy of this wavelength resolution. Each emission line source is placed at a random position in the field, which introduces the same uncertainties on the wavelength solution as seen in real data, including unknown

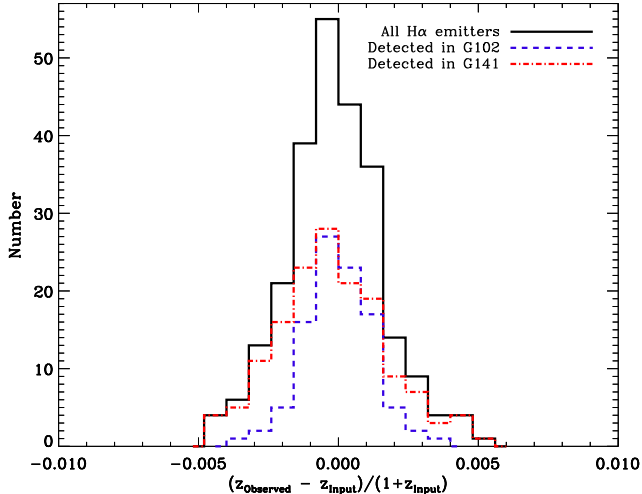


FIG. 4.— Histogram of redshift accuracy for $H\alpha$ -emitters taken from the simulations, where the accuracy is defined as $(z_{\text{observed}} - z_{\text{input}})/(1 + z_{\text{input}})$. The solid black histogram is all $H\alpha$ emitters, the dashed red histogram is those emitters found only in the G102 grism, and the dot-dashed blue histogram is the emitters found only in the G141 grism.

absolute positions and inexact object sizes. While this is not a measurement of the absolute wavelength accuracy – the model spectra are put in and taken out with the same software (aXe) and the same assumed wavelength solution – it is a reasonable test of the accuracy one can expect with this pixel sampling, extraction method, and signal-to-noise.

We removed the emission lines flagged because the reviewers could not agree on a redshift and then applied our S/N cut of 5 and EW cut of 40 Å. We found that going to even higher S/N and larger EW made almost no difference in the redshift accuracies we derived. For this analysis we are not interested in the catastrophic errors, which represent contamination of false lines in our samples rather than a real reflection of redshift accuracy, so we removed any objects with errors in $1+z > 0.5\%$. We discuss issues of contamination of false sources in Section 3.3. We further note that there is an error in the aXe process of inserting and removing user-generated spectra that incorrectly shifts the output wavelength calibration by a single pixel, corresponding to 24 Å in G102 and 46 Å in G141, which we have removed from all further analysis.

In Figure 4, the histogram of $(z_{\text{observed}} - z_{\text{input}})/(1 + z_{\text{input}})$ shows that the results are strongly peaked around zero. The median offset is -0.0002 with a standard deviation of 0.0017, or roughly 0.2% accuracy in redshift. Modeling of baryonic acoustic oscillations suggests that the redshift accuracies required for such an experiment are more like 0.1% (Wang et al. 2010), which is also the requirement for both the *Euclid* and *WFIRST* missions. However, it is important to recall that the WISP redshifts are a combination of two different near-infrared grisms (G102 and G141) with two different resolutions ($R \sim 210$ and $R \sim 130$). If we split the redshift accuracy histograms by the grism from which it came, we find the higher resolution grism reaches accuracies of 0.13% (as opposed to 0.19% in G141), demonstrating that 0.1% redshift accuracy is possible if the wavelength resolution

$R > 200$.

It is important to note that the lack of sub-pixel dithering of the parallel observations prevents any meaningful resampling of pixels along the direction of the wavelength dispersion. Such resampling would provide a small improvement in the overall wavelength resolution and would therefore also potentially increase the redshift accuracies that are possible.

3.3. False Emission Line Contamination

Identifying emission lines in grism spectroscopy fields without dithering or field rotation is a challenging task. Even the well-behaved WFC3 near-infrared arrays still have cosmic rays, hot pixels, and other phenomena that can mimic real emission lines. Therefore as we approach the detection threshold there is a real chance of contamination of our $H\alpha$ line sample by false emission lines. To investigate this further we look again to the simulation data. For the completeness calculation, we track whether an emission line galaxy is detected and placed into our final emission line list. There is no requirement that input and output redshifts must match. A mismatched redshift indicates contamination. While an emission line was found, it is clearly not identical to the emission line that was input. We label all extracted simulated spectra with a difference between input and output $(1+z)$ of more than 1% as contamination.

Of the 364¹ simulated $H\alpha$ emission lines that meet all extraction criteria ($S/N > 5$, $EW > 40$ Å), 312 are good emission lines found at the input redshift, a successful extraction rate of 85.7%. An additional 21 emission lines are at the correct input redshift if we assign them to be [OIII] rather than $H\alpha$, for a contamination of $H\alpha$ emission lines by [OIII] of 5.8%. For the remaining lines there are no alternative emission lines with which they could be associated, so they are contamination of non-emission lines to the sample. That gives us two contamination rates for our sample: 8.5% contamination by false emission lines and 14.3% total contamination rate of $H\alpha$ emission lines by the combination of [OIII] and false emission lines.

This false emission line contamination rate decreases slightly as we increase the cut-offs of either equivalent width or signal-to-noise of the line fluxes, but contamination rate never improves to much less than 10%. For instance, whether we raise the equivalent width cut-off from 40 Å to 200 Å or raise the the signal-to-noise line flux cut-off from 5 to 20, the false emission line contamination rate drops by only 3.5%, to 10.8% total contamination.

We note that one other potential contaminant is [OII] 3727 Å. [OII] emission is generally faint, with fluxes around 40% those of [OIII] 5007+4959 Å. For redshifts where [OII] and [OIII] both fall into the detectable near-infrared wavelength range ($1.3 < z < 2.3$), if we detect [OII], we always detect [OIII] as well. There are some rare cases where [OII] 3727 Å can be as much as 30% brighter than [OIII], but that [OII]/[OIII] ratio is not large enough to make any significant number of [OIII] emitters undetectable. Therefore we do not expect any contamination

¹ This number is slightly less than the 380 simulated emission lines referred to in Section 3.1, as it does not contain 16 weak $H\alpha$ emitters that were found only because of their [OIII] emission.

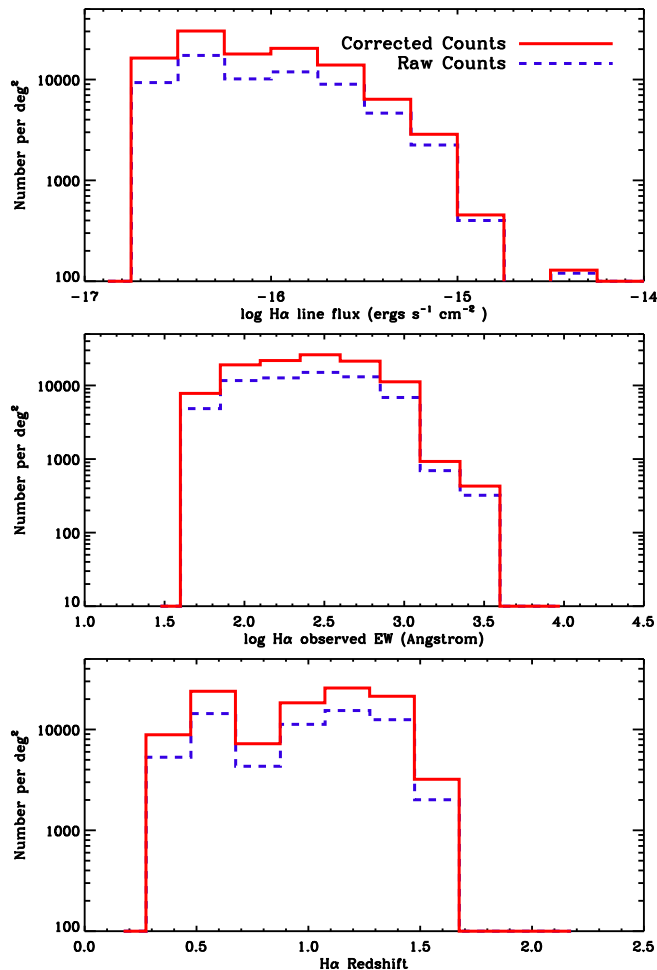


FIG. 5.— Histogram of all detected $H\alpha$ line emitters as a function of *top*) line flux, *middle*) observed equivalent width, and *bottom*) redshift. The dashed blue lines are the raw, uncorrected counts, while the solid red lines are the counts after the correction for completeness.

from $[\text{OII}]$ 3727 Å below a redshift of $z < 2.3$. However, the assumption that all single emission lines are $H\alpha$ could potentially lead us to miss a population of very high redshift ($z > 2.3$) $[\text{OII}]$ emitters. These high redshift $[\text{OII}]$ -emitters would have to be very luminous, i.e., more than 5 times the L_* found for $[\text{OII}]$ at $z = 1.47$ (Ly et al. 2007), and should therefore be quite rare. By $z = 2$, the number density of $[\text{OII}]$ -emitters has already dropped below 500 deg^{-2} , suggesting it is unlikely there could be more than 3-5 $z > 2.3$ $[\text{OII}]$ -emitters hidden in our $H\alpha$ sample.

We do not make any separate corrections for these false emission line contamination rates in our analysis. The completeness corrections we apply are based on all the extracted emission lines from the simulations, including the contaminating lines. While the contaminating lines artificially inflate the number of model emission line galaxies recovered, which reduces the derived completeness corrections, we expect the same contamination rates in the actual data. If we used completeness corrections that did not include contaminating lines, we would incorrectly produce final number counts that were too large. By leaving the contaminating lines in our completeness derivation, we produce completeness corrections that si-

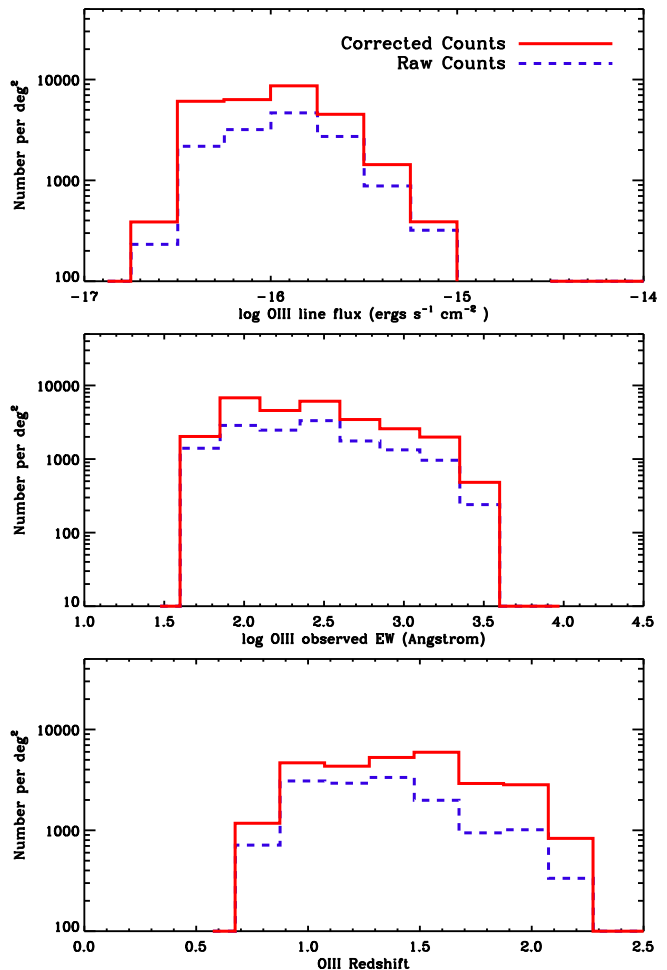


FIG. 6.— Histogram of all detected $[\text{OIII}]$ line emitters as a function of *top*) line flux, *middle*) observed equivalent width, and *bottom*) redshift. The dashed blue lines are the raw, uncorrected counts, while the solid red lines are the counts after the correction for completeness. We note that the faintest $[\text{OIII}]$ flux bins consist mostly of secondary, fainter lines that have only been identified and included because they are companions to brighter $H\alpha$ emission lines. We make no attempt to correct for this incompleteness, choosing instead to restrict our analysis to the brighter lines.

multaneously account for the effects of both incompleteness and contaminating lines. To put it another way, the completeness corrections we use are $\sim 15\%$ smaller than they would otherwise be because of the extra emission lines we added due to contamination.

4. EMISSION LINE NUMBER COUNTS

The most numerous emission line seen by far is that of $H\alpha$, which makes up two thirds of all those observed. Of the 996 $H\alpha$ emission lines with EWs > 40 Å and $S/N > 5$, 577 (58%) are identified from a single line. While identifying $H\alpha$ emission from a single line introduces the possibility of a misidentification, our simulations (see Section 3.3) demonstrate that this affects no more than 6% of our emission line galaxies. Since virtually all the misidentifications are single emission lines, this implies that roughly 10% of our single $H\alpha$ emission lines are actually not $H\alpha$ at all, but instead misidentified $[\text{OIII}]$. While far from negligible, the level of $[\text{OIII}]$ emission line contamination down to the flux levels probed

by this work ($3\text{--}5 \times 10^{-17}$ ergs $\text{s}^{-1} \text{cm}^{-2}$) remains small enough (10% of single emission lines, 6% of all lines) that it can be easily accounted for in the statistical analysis.

In Figures 5 and 6, we plot the sky density for H α and [OIII] versus flux, equivalent width, and redshift in both the original raw counts and those corrected for completeness. Here we can see that there are significant completeness corrections applied across the entire range of fluxes.

4.1. Emission Line Number Densities

To derive the number density of the H α emission lines in our survey, we employed the V_{MAX} method (Felton 1977), in which we derive the maximum distance for which an emission line of that absolute luminosity could be detected, depending on the flux limits of each field, and then translate that to a volume, V_{MAX} . This can be translated into a density:

$$\delta_{gal} = \frac{4\pi}{\Omega} \sum C(SNR, EW) \frac{1}{V_{MAX}} \quad (1)$$

where $C(SNR, EW)$ is the completeness correction for each detected emission line galaxy, as a function of signal-to-noise and equivalent width. We scale the volume of the entire sphere of the sky by the angular area observed, $4\pi/\Omega$, to reach the volume density for each object, δ_{gal} . Then we add up all the δ_{gal} to get the total volume densities, which we then use for derivation of the luminosity functions (see Section 4.3).

Similarly, we also calculate area number densities, deriving an A_{MAX} for each source. A_{MAX} is the total angular area from the survey for which the emission line flux is greater than that of the 5σ line limit of the field. For the brighter emission lines, A_{MAX} will simply equal the angular area of the entire survey (29 fields in this case). Similar to the V_{MAX} method, once the A_{MAX} 's are determined we add up all the $1/A_{MAX}$ values to determine the area number density. For calculation of both V_{MAX} and A_{MAX} , the detector area used is roughly two thirds ($\sim 3 \text{ arcmin}^2$) of the total area of the WFC3 IR chip (4.65 arcmin^2), as objects are lost to the edges where either the 1st order spectrum falls off the chip (right side) or there are no direct images of galaxies available (left side).

The primary surveys of the future near-infrared grism space missions, *Euclid* (Laureijs et al. 2012) and *WFIRST* (Green et al. 2012, Dressler et al. 2012), will both cover thousands of square degrees to depths significantly shallower than the WISP program. The *Euclid* wide spectroscopic survey will cover 15,000 square degrees over a wavelength range of $1.1\text{--}2 \mu\text{m}$, with a resolution of $R=250$ and a 3.5σ line flux depth of 3×10^{-16} ergs $\text{s}^{-1} \text{cm}^{-2}$. At time of publication, the *WFIRST* mission is still considering several competing designs, but the primary spectroscopic mission will likely cover at least 2000 square degrees at a resolution of $R=600$, down to a 7σ line flux depth of 1×10^{-16} ergs $\text{s}^{-1} \text{cm}^{-2}$. The wavelength range for *WFIRST* will likely start between 1.3 and $1.5 \mu\text{m}$ and end somewhere between 2 and $2.4 \mu\text{m}$. While this paper focuses on comparisons and predictions for the future shallow wide surveys of *Euclid* and *WFIRST*, it should be noted that both missions will certainly contain deeper surveys done over less area. For instance, the *Euclid* mission plan contains at least two

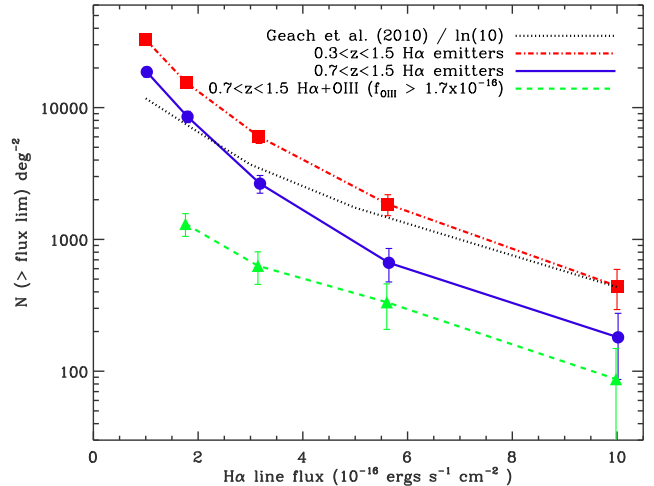


FIG. 7.— Cumulative number count density as a function of H α line flux. The red squares and dotted-dashed line are all the $0.3 < z < 1.5$ H α emitters, the blue circles and solid line are just H α emitters between $0.7 < z < 1.5$, while the green triangles and dashed line are H α emitters with [OIII] line emission greater than 1.7×10^{-16} ergs $\text{s}^{-1} \text{cm}^{-2}$ (approximately 2σ for the planned *Euclid* line flux limits). The dotted black line is the number count density prediction of Geach et al. (2010), divided by $\ln(10)$.

20 square degree deep fields with planned depths very similar to the observations for the WISP program, with line flux limits around 5×10^{-17} ergs $\text{s}^{-1} \text{cm}^{-2}$.

In Figure 7, we plot cumulative number counts versus limiting flux for the WISP survey, covering the primary range of interest ($1\text{--}10 \times 10^{-16}$ ergs $\text{s}^{-1} \text{cm}^{-2}$) of these future surveys. Completeness corrections have been applied to all points. We present three cumulative number measurements: total H α emitters (red squares), $0.7 < z < 1.5$ H α emitters (blue circles), and $0.7 < z < 1.5$ H α emitters for which [OIII] is also detected (green triangles). At the bright flux end (10^{-15} ergs $\text{s}^{-1} \text{cm}^{-2}$) we find a factor of 1.5 times more H α emission lines at $0.3 < z < 0.7$ than at $0.7 < z < 1.5$. As we approach fainter fluxes the percentage of high redshift objects increases, with the number of $0.7 < z < 1.5$ sources exceeding those at $0.3 < z < 0.7$ around 2×10^{-16} ergs $\text{s}^{-1} \text{cm}^{-2}$.

The WISP survey reaches shorter wavelengths ($0.85 \mu\text{m}$) than presently planned for these future space missions. The *Euclid* short wavelength limit, $1.1 \mu\text{m}$, translates into an H α redshift of $z=0.7$, so we use the $0.7 < z < 1.5$ cumulative number counts to predict what these future space missions will find, noting that the *WFIRST* number counts will be somewhat lower depending on the exact low wavelength cut-off used. The $1.65 \mu\text{m}$ WISP cut-off is a shorter long wavelength cut-off than the $2 \mu\text{m}$ or better planned for these future missions, but that only means the WISP survey is not sensitive to the highest redshift H α emitters. Because of the steep fall-off in number counts with redshift for the flux limits being planned, it is unlikely the cumulative H α number counts presented will be much different even with longer wavelength sensitivity.

For comparison to our $0.7 < z < 1.5$ cumulative number counts, we plot the $0.75 < z < 1.9$ number counts derived from the study of Geach et al. (2010), which is mostly based on *HST* NICMOS grism and near-IR narrow band number counts (Shim et al. 2009, Geach et al. 2008,

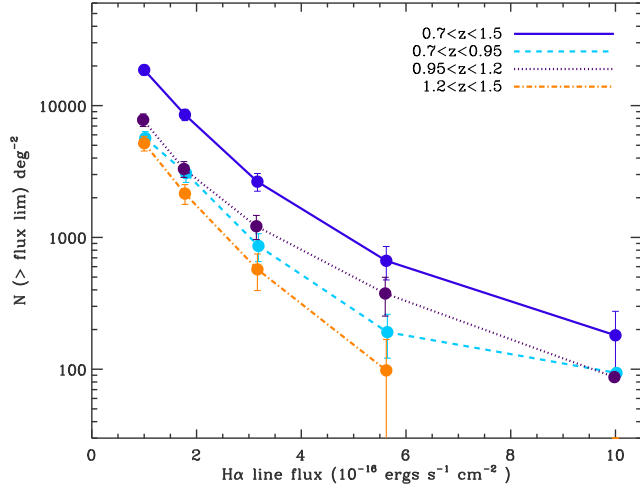


FIG. 8.— Cumulative number count density as a function of $H\alpha$ line flux split into different redshift bins from $0.7 < z < 1.5$. The solid blue line is all emitters from $0.7 < z < 1.5$ and is unchanged from Figure 7. The dashed light blue line is $0.7 < z < 0.95$, the dotted purple line is $0.95 < z < 1.2$, and the dotted-dashed orange line is $1.2 < z < 1.5$.

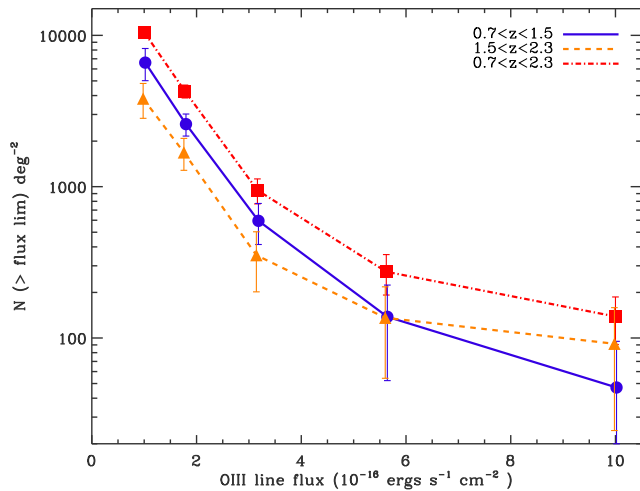


FIG. 9.— Cumulative number count density as a function of $[OIII]$ line flux, split into different redshift bins. The red squares and dotted-dashed line is all emitters from $0.7 < z < 2.3$, the blue circles and solid line are the number density counts from $0.7 < z < 1.5$, while the orange triangles and dashed line are $1.5 < z < 2.3$.

Sobral et al. 2009). We have decreased the result from the published article by a factor of $\ln(10)$ to account for an error in the published values of Φ_* used, a result of improperly converting $\Phi(\log L)$ luminosity functions to the more standard $\Phi(L)$ luminosity functions. Once we account for this offset, we find agreement between their NICMOS-derived cumulative distribution and our distribution from WISP at the faint end, although there is some significant deviation brighter than 5×10^{-16} ergs $s^{-1} cm^{-2}$, where WISP detects roughly a factor of 2-2.5 fewer sources. We find approximately 2500 (18,500) $H\alpha$ emitters deg^{-2} in the redshift range $0.7 < z < 1.5$ down to $3 (1) \times 10^{-16}$ ergs $s^{-1} cm^{-2}$.

To predict the number of multiple emission line ($H\alpha + [OIII]$) sources a future near-infrared slitless spectroscopy space mission could expect to find per square degree, one

must first choose a flux limit down to which $[OIII]$ will also be detectable. This detection limit will vary depending on survey depth and secondary line reliability requirements. We can start with the presently planned *Euclid* mission 3.5σ detection limit of 3×10^{-16} ergs $s^{-1} cm^{-2}$. If we make the further assumption that one could reach a lower significance limit of 2σ for a secondary line if one already had a higher confidence line in hand, then one could detect $[OIII]$ flux down to 1.7×10^{-16} ergs $s^{-1} cm^{-2}$. We apply this $[OIII]$ flux limit to the green cumulative count line in Figure 7, producing a prediction for *Euclid* for the number density of emission line galaxies where both $H\alpha$ and $[OIII]$ will be detected. Down to an $H\alpha$ flux of 3×10^{-16} ergs $s^{-1} cm^{-2}$ we find that roughly 24% of the $0.7 < z < 1.5$ $H\alpha$ -emitters are also detected in $[OIII]$, or 600 $H\alpha + [OIII]$ emitters per square degree. A higher limit on the $[OIII]$ flux will obviously exclude more multiple emission line objects from the final counts. For instance, if we require the $[OIII]$ and $H\alpha$ line flux to both be greater than 3×10^{-16} ergs $s^{-1} cm^{-2}$, then the density of $H\alpha + [OIII]$ emitters drops by half, down to around 280 per square degree.

With 314 $H\alpha$ emission lines at $z > 0.7$ with fluxes above 10^{-16} ergs $s^{-1} cm^{-2}$, we have enough emission lines to break down the cumulative number counts into even smaller redshift bins in Figure 8. This more detailed redshift breakdown allows us to examine the evolution of the number counts that will be available to these future near-infrared slitless spectrographs in space. At a flux of 10^{-15} ergs $s^{-1} cm^{-2}$ the $0.7 < z < 1.5$ $H\alpha$ emission line galaxies are split roughly equally between $0.7 < z < 0.95$ and $0.95 < z < 1.2$. However, by 6×10^{-16} ergs $s^{-1} cm^{-2}$, the emitters from the $0.95 < z < 1.2$ redshift range outnumber those from $0.7 < z < 0.95$ by a factors of 1.5-2 and remain more numerous down to fainter fluxes. Our highest redshift bin, $1.2 < z < 1.5$, has no emission lines as bright as 10^{-15} ergs $s^{-1} cm^{-2}$ and is not a significant percentage of the emission line sample until fluxes less than $\sim 3 \times 10^{-16}$ ergs $s^{-1} cm^{-2}$.

We can also look at the number densities of the $[OIII]$ emission lines on their own in Figure 9. Over the same range of line fluxes, the number counts of $[OIII]$ emitters initially rise much more slowly than the numbers of $H\alpha$ -emitters, before rising quickly for fluxes fainter than 3×10^{-16} ergs $s^{-1} cm^{-2}$. At 10^{-15} ergs $s^{-1} cm^{-2}$, there are 3 times more $H\alpha$ than $[OIII]$ emission lines, but by 6×10^{-16} ergs $s^{-1} cm^{-2}$ that number density difference has increased to a factor of 7. Then, thanks to the steep rise of the fainter $[OIII]$ -emitters, this number density disparity rapidly shrinks and returns to a factor of 3 for line fluxes of 10^{-16} ergs $s^{-1} cm^{-2}$. This steep rise in the relative $[OIII]$ number density can also be seen in the decreasing $H\alpha/[OIII]$ ratio we measure for fainter line fluxes (see Section 4.2 below).

We find roughly 1.5 times as many $0.7 < z < 1.5$ $[OIII]$ emitters, where $H\alpha$ can also be identified in the WISP data, as $[OIII]$ emitters found at the higher $1.5 < z < 2.3$ redshifts. This is after accounting for the extra incompleteness $[OIII]$ suffers at the higher redshift (see Section 3.1.1). In the actual raw counts we find 3 times as many $0.7 < z < 1.5$ $[OIII]$ emitters. This number difference between redshifts remains fairly constant over the 1.5×10^{-16} ergs $s^{-1} cm^{-2}$ flux range. In the data we

see an unexpected crossover towards the brightest end, with the highest redshift emitters becoming the most populous. However, the number statistics here are quite poor, with only 9 total [OIII] emitters covering the $5\text{--}10 \times 10^{-16} \text{ ergs s}^{-1} \text{ cm}^{-2}$ flux range, split into the two redshift bins. Within the error bars, we find the number counts are consistent with no significant change in the number ratio between the high and low redshift [OIII] emitters over the entire flux range. This relatively steady number count ratio across a wide range of redshifts suggests that the luminosity of the typical [OIII] emitter (L_*) is increasing strongly with redshift, something we examine further when we look at the [OIII] luminosity function in Section 4.3.

4.2. $H\alpha$ /[OIII] Ratio

Over the near-infrared wavelength range probed by the WISP survey, $0.85\text{--}1.65\mu\text{m}$, the vast majority of the emission lines observed are either $H\alpha$ or [OIII]. When other emission lines are identified they are always found at the same time as one of those two lines, largely because these two emission lines are almost always significantly stronger than the other available lines. Besides the possibility of a rare [OII] emitter (see Section 3.3 above), our simulations suggest that the assumption that all single line emitters are $H\alpha$ mainly results in the misidentification of [OIII] emission. While these failed identifications only effect 6% of $H\alpha$ lines, it has a large effect on the high redshift ($z > 1.5$) [OIII]-emitters, where we lose nearly 50% from our final sample.

The future near-infrared grism space missions are likely to suffer similar single emission line misidentification issues. Increased wavelength resolution will certainly aid in identification, as a resolved [OIII] $5007+4959 \text{ \AA}$ doublet will not be confused with $H\alpha$. However, for grism spectroscopy wavelength resolution is not the only limiting factor. If the emitting region is large in spatial extent it will smear out the doublet, effectively lowering the available wavelength resolution. While the median galaxy radius of our sample is only $0.2''$, the future wide-area grism missions will reach shallower flux depths and therefore should find larger objects, as there is a strong correlation between line flux and galaxy size (see Figure 10).

Down to $3 \times 10^{-16} \text{ ergs s}^{-1} \text{ cm}^{-2}$ and limiting our analysis to redshifts of $z > 1.2$ (where $H\alpha$ /[OIII] confusion becomes an issue at $1.1\mu\text{m}$), we find the radius of the median object increases 50% to $0.3''$. While the sample of objects with both high fluxes and high redshifts is small, a full 25% (4 of 16) have radii larger than $0.5''$. Fortunately the pixel scale for the *Euclid* mission will be $0.3'' \text{ pixel}^{-1}$, more than twice that of the IR WFC3, which should greatly mitigate the degradation of wavelength resolution caused by extended sources. While the exact pixel scale for *WFIRST* detectors remains uncertain, it will likely be close to that of the WFC3 IR channel, $0.13'' \text{ pixel}^{-1}$. However, the proposed *WFIRST* wavelength resolution ($R=600$) is large enough that the wavelength smearing should not prevent identification of the [OIII] $5007+4959 \text{ \AA}$ doublet in most cases.

To investigate the likelihood of single emission line confusion further, we plot the ratio of $H\alpha$ /[OIII] as a function of $H\alpha$ flux in Figure 11. We limit our redshift range to

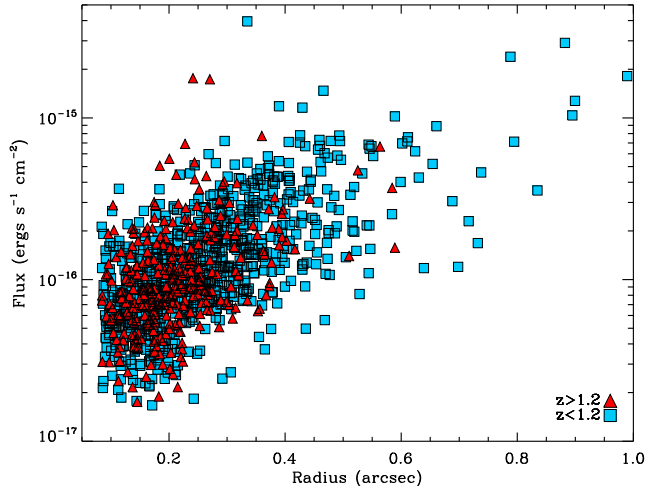


FIG. 10.— Flux versus radius for our entire sample of line emitters, $EW > 40 \text{ \AA}$ and $S/N > 5$. The flux given is $H\alpha$ emission except in cases where $H\alpha$ is not detected (mostly at $z > 1.5$), in which case the flux presented is [OIII]. Emission line galaxies with redshifts of $z > 1.2$ are red triangles, while those with redshifts $z < 1.2$ are blue squares.

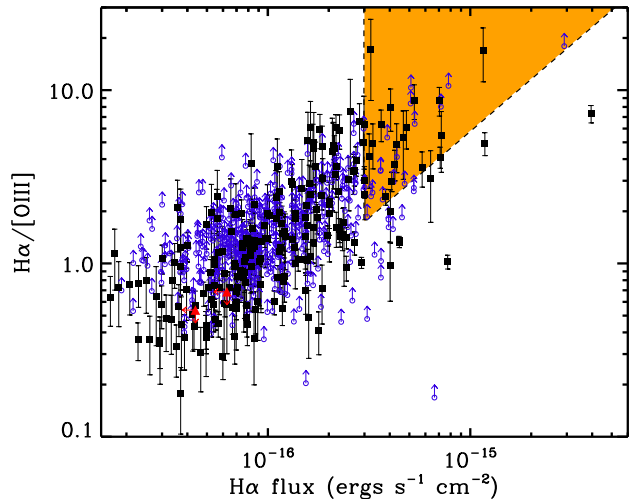


FIG. 11.— Ratio of $H\alpha$ divided by [OIII] line flux versus $H\alpha$ flux for all detected $0.7 < z < 1.5$ line emitters. Solid black squares are sources in which both lines are detected. The empty blue circles are sources where only $H\alpha$ is detected and are lower limits, while the red triangles are the two sources where only [OIII] has been detected, with its two arrows pointing towards the quadrant those points must really lie. The orange wedge represents the area where one would expect to find only a single $H\alpha$ emission line, assuming an $H\alpha$ detection limit of $3 \times 10^{-16} \text{ ergs s}^{-1} \text{ cm}^{-2}$ (planned *Euclid* survey limit) and a fainter [OIII] detection limit of $1.7 \times 10^{-16} \text{ ergs s}^{-1} \text{ cm}^{-2}$.

that for which both $H\alpha$ and [OIII] can be detected. Upper limits are $2\text{-}\sigma$, assuming the FWHM of the line for which a limit is being derived is the same as for the measured emission line. We find only two cases where [OIII] is detected without $H\alpha$.

The upper left part of Figure 11, where the $H\alpha$ /[OIII] ratio is large and $H\alpha$ fluxes are small, is empty of sources because that is where the flux limits of the survey prevent sampling. If the high $H\alpha$ /[OIII] ratios we see at brighter fluxes continue down to fainter fluxes, then pre-

sumably we would find many of the lower limits moving into that region if we were sensitive enough to detect such faint [OIII] fluxes. The lower right portion of Figure 11, where $H\alpha/[OIII]$ ratio is small and the $H\alpha$ fluxes are bright, is similarly devoid of objects, but that region is not excluded by our sensitivity limits. There is a real scarcity of low $H\alpha/[OIII]$ sources at the bright flux limits. Excluding three lower limits, we find none of the 58 galaxies with $H\alpha$ fluxes greater than 3×10^{-16} ergs s $^{-1}$ cm $^{-2}$ have ratios of $H\alpha/[OIII] < 0.95$.

While the WISP survey does not cover the same wavelength range as the future space near-infrared grism missions (WISP goes to shorter wavelengths while the future missions will go longer), it does give us a rough estimate of the percentage of single line emitters those missions are likely to find. The exact percentage of single line emitters will depend on their final flux limits and criteria for establishing the reality of an emission line. For this example we again choose the presently planned detection limit for *Euclid* (3.5σ limit of 3×10^{-16} ergs s $^{-1}$ cm $^{-2}$) and assume a secondary line only needs to be detected at a 2σ significance (1.7×10^{-16} ergs s $^{-1}$ cm $^{-2}$). The shaded orange region on Figure 11 shows the region for which only single line emitters would be expected for these sets of limits. We find that at least 60% (35/58) of sources with emission lines brighter than 3×10^{-16} ergs s $^{-1}$ cm $^{-2}$ will be single line emitters in future surveys. This single line discovery rate could potentially be as high as 80% if all the lower limits presented actually lie within the single line discovery region.

We can also look at a sample where the redshift is $z > 1.2$, as that would better reflect the range over which [OIII] would be detectable if the lower wavelength cut-off is the $1.1 \mu\text{m}$ cut-off of *Euclid* rather than the $0.85 \mu\text{m}$ of the WISP survey. The number of bright emitters is much smaller (12) but the percentage of expected single line emitters, 67–83%, is virtually the same as when we included the lower redshifts emitters.

Our analysis assumes all the single emission lines are $H\alpha$, which we know to be incorrect roughly 6% of the time. Therefore it is possible that approximately 2 of the 31 single line emitters in that flux range could be low $H\alpha/[OIII]$ sources, although if their true redshifts are greater than $z = 1.5$ then their $H\alpha$ fluxes and $H\alpha/[OIII]$ ratios are not constrained. It is important to emphasize that of the 25 sources with bright fluxes where we detect both $H\alpha$ and [OIII], *none* of them have $H\alpha/[OIII] < 1$. There is no obvious reason why we would be missing all the galaxies with low $H\alpha/[OIII]$ from $0.7 < z < 1.5$, unless the ratio is so low that we lose the ability to detect $H\alpha$. However that would require an unlikely large gap in the $H\alpha/[OIII]$ ratio, making all galaxies either strong $H\alpha$ or strong [OIII]-emitters, with none in between.

Regardless of the exact quantity of contamination from single line [OIII] emission, clearly $H\alpha/[OIII] < 1$ sources are much rarer at the bright fluxes that future near-infrared grism missions will probe than in our fainter sample. Therefore the assumption that all single line emitters are $H\alpha$ should produce very few contaminating interlopers for these space missions, although further data is required to better establish exactly what the [OIII] contamination rate is.

The trend of increasing $H\alpha/[OIII]$ ratio with $H\alpha$ flux is

a result of the known correlation between the $H\alpha/[OIII]$ ratio and $H\alpha$ luminosity previously reported by WISP (Domínguez et al. 2013). Their analysis also indicates that dust extinction increases with $H\alpha$ luminosity, meaning that dust extinction is suppressing [OIII] emission more at the bright luminosity end. However, the trend of stronger relative [OIII] with fainter $H\alpha$ luminosity is far stronger than their measured effects of extinction. The dominant determinant of the $H\alpha/[OIII]$ ratio is most likely the metallicity, as the [OIII] 5007 Å/Hβ ratio strongly correlates with metallicity in the local universe (i.e., Liang et al. 2006). Metallicity is known to correlate with mass and luminosity (Tremonti et al. 2004, Kobulnicky & Kewley 2004), so it is not surprising that the brightest $H\alpha$ emitters, which tend to be the most luminous in the continuum as well, would also have higher $H\alpha/[OIII]$ ratios.

4.3. Luminosity Functions

Using the total volume densities derived for each luminosity bin (see Section 4.1) we are able to plot $H\alpha$ luminosity functions in Figure 12. We have split the $H\alpha$ emission line luminosity function into two redshift ranges, $0.3 < z < 0.9$ and $0.9 < z < 1.5$. We chose to split the sample at $z=0.9$ as that divides the detected $H\alpha$ emission lines by the grism with which they were detected (the dividing line between G102 and G141 is $\sim 1.2 \mu\text{m}$), which also has the added benefit of producing nearly even sample sizes (451 $0.3 < z < 0.9$ versus 534 $0.9 < z < 1.5$). We make no correction for dust extinction, but there is a correction factor of 0.71 applied to the luminosities to account for NII contamination. Our best-fit Schechter parameters are presented in Table 2.

Generally we find that the $0.9 < z < 1.5$ luminosity function is slightly higher at the faint luminosity end than the previous NICMOS grism studies, such as those by Shim et al. (2009) and Yan et al. (1999). This slight surplus in number density shrinks as the $H\alpha$ luminosities become brighter, before dropping below the previous NICMOS surveys by $\log L = 42.5$. The faint end differences are likely explained by the greater sensitivity of the WISP survey to lower line equivalent widths (EWs). We measure lines down to an observed EW of 40 Å, while the typical NICMOS grism survey did not find lines much below 80–100 Å (Shim et al. 2009). We find that 15% of our total unweighted sample has EWs less 80 Å. The redshift sampling difference ($0.7 < z < 1.4$ with NICMOS versus $0.9 < z < 1.5$ with WFC3) is not sufficiently different to effect the luminosity function comparison.

We also find our $0.9 < z < 1.5$ number densities to be consistently higher ($1.3\text{--}2\times$) than the $z=1.47$ number densities derived from the narrow band $H\alpha$ surveys (Sobral et al. 2012). The redshifts sampled by Sobral et al. (2012) – at $z=0.84$ and 1.47 – straddle the sampled range of our high redshift sample, so if all the luminosity functions were consistent, then the WISP luminosity function ought to lie between the two Sobral et al. (2012) distributions, not above them both. The HiZELS data sample down to very similar EWs (25 Å), so that is not a likely source of the difference. Neither data sample has made any attempt to remove AGN, so that can not be a source of difference either. Our lower redshift $0.3 < z < 0.9$ sample, on the other hand, almost perfectly overlaps the

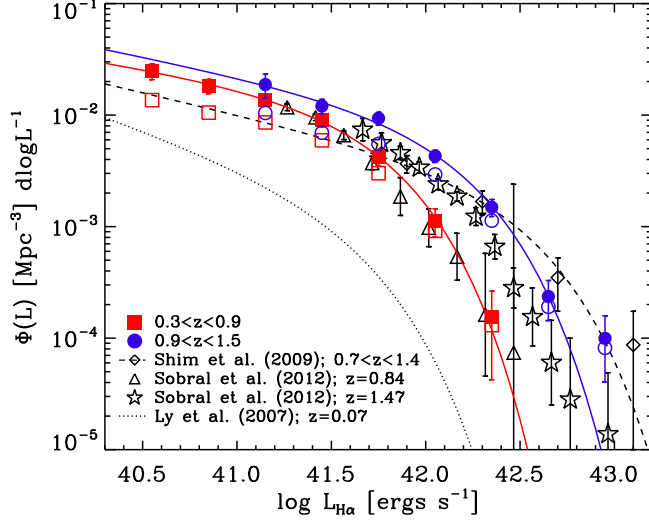


FIG. 12.— $H\alpha$ luminosity function derived from WISP emission line sample. The red squares are line emitters from $0.3 < z < 0.9$, while the blue circles are line emitters from $0.9 < z < 1.5$. Best-fit Schechter functions have been overlaid on top with solid blue and red lines. The empty circles and squares are raw counts, while the solid circles and squares have been corrected for completeness. The diamonds and dashed line are the measured points and Schechter fit from the NICMOS grism study of Shim et al. (2009) for $0.7 < z < 1.4$. The triangles and stars are from the HiZELS narrow band study (Sobral et al. 2012) at $z=0.84$ and $z=1.47$ respectively. The dotted line is the $z=0.07$ $H\alpha$ luminosity function (Ly et al. 2007).

Sobral et al. (2012) narrow band $z=0.84$ number counts. However, with a median $z=0.6$ for our lower redshift $H\alpha$ -emitters and the observed trend of rising luminosity functions across these redshift ranges, one would expect to find our $H\alpha$ counts slightly below those of the $z=0.84$ narrow band survey. That the number densities instead overlap suggests that the WISP grism survey is finding slightly more line emitters than the narrow band, although the absolute differences are small. The expected cosmological variance for the Sobral et al. (2012) narrow band counts is on the order of 20% (Trenti & Stiavelli 2008), so that can not entirely explain the difference.

Regardless of how our sample selection may differ from other surveys, we can robustly compare how the luminosity function evolves within the WISP survey as we use the same methodology for selection and completeness corrections. It appears that most of the evolution from $z=0.3$ - 1.5 takes place at the bright end of the luminosity function. Within the errors, the luminosity functions are converging below $\log L=41$. However, with only two low luminosity bins for the high redshift sample, this low luminosity convergence is not definitive. Further discussion of the $H\alpha$ luminosity functions, their implied star formation rates, and the evolution of the star formation density, will be presented in a separate paper (Bunker et al. 2013, in prep).

We also present the [OIII] luminosity functions in Figure 13 along with their accompanying best-fit Schechter parameters in Table 1. For [OIII] we split luminosity functions into two redshift ranges, $0.7 < z < 1.5$ and $1.5 < z < 2.3$, which are the highest redshifts for which the [OIII] luminosity function has been determined to date. The lower redshift bins cover the range over which we expect to also find the $H\alpha$ line within the grism spec-

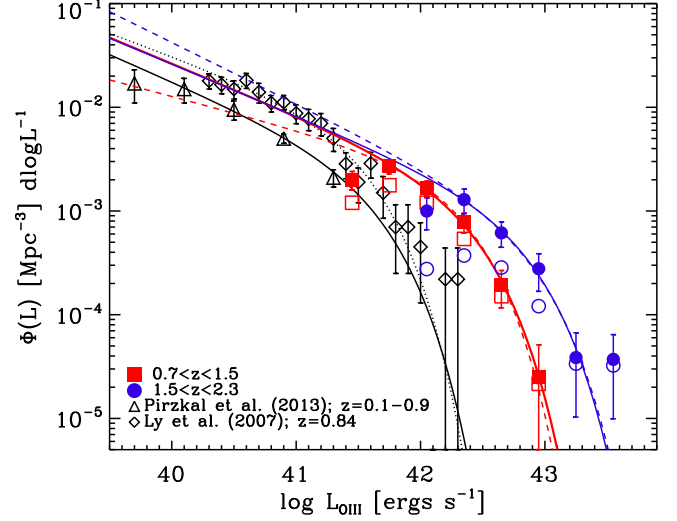


FIG. 13.— [OIII] luminosity function derived from WISP emission line sample. The red squares are [OIII] emitters from $0.7 < z < 1.5$, while the blue circles are $1.5 < z < 2.3$. We plot Schechter function fits with both a fixed $\alpha = -1.5$ (solid lines) and one where we allow α to vary (dashed lines). The empty circles and squares are raw counts, while the solid circles and squares have been corrected for completeness. The triangles and solid line fit are from the $z=0.1$ - 0.9 PEARS Grism Survey (Pirzkal et al. 2012), while the diamonds and dotted line fit are from the $z=0.84$ narrow band study of Ly et al. (2007).

tra. For $z > 1.5$, $H\alpha$ is redshifted beyond $1.65\mu\text{m}$, leaving [OIII] as the most powerful detectable line in the grism spectrum. The total sample sizes are 192 [OIII]-emitters at $0.7 < z < 1.5$ versus 58 at $1.5 < z < 2.3$.

As remarked in Section 3.1.1, the [OIII] number densities require higher completeness corrections than for $H\alpha$. Even after application of these additional larger corrections, we still find that the lowest luminosity bin for each redshift range appears low, indicating that there is some incompleteness for which we are not accounting. One possibility is that the number of mis-identified single line [OIII]-emitters is even larger at the faintest ends than our simulations indicate. For instance, our simulations assume $H\alpha$ /[OIII] ratios similar to the emission line sources that we find and can measure. Therefore, if a population of faint, low $H\alpha$ /[OIII] sources exist, we would be underestimating the number of single line mis-identifications at the lower redshifts (at higher redshifts the $H\alpha$ /[OIII] ratio does not matter as we can not see $H\alpha$ at all). Regardless of the reason for the low faintest bin, we exclude them from the Schechter fits and further analysis.

Comparing our [OIII] luminosity functions to those derived at lower redshift (Pirzkal et al. 2012, Ly et al. 2007), we see a strong increase in L_* with redshift along with decrease in Φ_* . However, our measured luminosity bins do not constrain α well. If we require the $0.7 < z < 1.5$ α to be the same as seen at low redshift ($\alpha=-1.5$), we find little significant change in Φ_* , with all the evolution in [OIII] from $z=0.7$ - 2.3 taking place in L_* .

5. SUMMARY AND CONCLUSIONS

We present near-infrared emission line number densities, line ratios, and luminosity functions, based on 29 fields from the WISP survey taken with both the

TABLE 2
LUMINOSITY FUNCTION BEST-FIT SCHECHTER PARAMETERS

Emission Line	Redshift Range	Φ_*	L_*	α
H α	$0.3 < z < 0.9$	-2.27 ± 0.11	41.72 ± 0.09	-1.27 ± 0.10
H α	$0.9 < z < 1.5$	-2.40 ± 0.12	42.13 ± 0.09	-1.34 ± 0.16
[OIII]	$0.7 < z < 1.5$	-3.00 ± 0.21	42.31 ± 0.17	-1.32 ± 0.36
[OIII]	$1.5 < z < 2.3$	-3.45 ± 0.40	42.88 ± 0.35	-1.59 ± 0.77
[OIII]	$0.7 < z < 1.5$	-3.15 ± 0.08	42.40 ± 0.08	-1.5 (fixed)
[OIII]	$1.5 < z < 2.3$	-3.37 ± 0.14	42.84 ± 0.11	-1.5 (fixed)

G102+G141 grism filters. With this dataset we find emission line galaxies *without any pre-selection bias*, over a large continuous epoch of cosmic time. At least two future space missions, *Euclid* and *WFIRST*, will also contain very large near-infrared grism surveys. The WISP survey is a perfect laboratory to predict what these future missions can expect to find.

We found the most significant potential issues with identifying emission lines from near-infrared grism spectroscopy to be:

- **Confusion of H α and [OIII] due to insufficient wavelength resolution**, which can lead to catastrophic redshift identification failures. When the signal-to-noise gets low enough, one can not necessarily depend on being able to distinguish the [OIII] doublet from a single emission line. This is particularly true in the case where the emission line region is spatially extended, which effectively degrades the wavelength resolution. This could potentially be a significant issue for shallower surveys, as the brighter emission line sources tend to also be larger in spatial extent. However, we found this line confusion to be almost entirely confined to the lower resolution ($R \sim 130$) G141 grism and not an issue for the higher resolution ($R \sim 210$) G102 grism. Additionally our simulations found that the higher grism resolution is also needed to achieve the 0.1% accuracy in $1+z$ required for baryonic acoustic oscillation experiments. We would therefore strongly recommend that future near-IR missions keep to wavelength resolutions above $R > 200$.
- **Contamination from overlapping spectra from bright sources**, which effects even bright, high signal-to-noise spectra. It alters the measured continuum, impacts the effectiveness of automatic line finding algorithms, makes it difficult to identify the correct host galaxy and emission line wavelength, and results in emission lines that are lost altogether. Roughly 5% of all our bright lines ($> 3 \times 10^{-16}$ ergs s $^{-1}$ cm $^{-2}$) are lost to overlapping bright source contamination. The use of multiple roll angles would greatly minimize these effects, particularly for the brighter, less densely-packed sources mostly being targeted by future missions.
- **Lack of dithering**, which not only greatly impacts our ability to mitigate cosmic rays, hot and warm pixels, and other artifacts that can mimic emission lines, but also prevents us from recovering the additional resolution that sub-pixel dithering can provide. With grism spectroscopy, this results in not only improved spatial resolution, but

also improved wavelength resolution, which helps to address the insufficient wavelength resolution issue already discussed above.

While WISP is sensitive to H α emitters down to $z=0.3$, both *Euclid* and *WFIRST* will likely have low wavelength cut-offs around $1.1 \mu\text{m}$ making them mostly sensitive to emission line galaxies at $z > 0.7$. We find that our cumulative number of H α galaxies at $0.7 < z < 1.5$ reaches 10,000 deg $^{-2}$ by an H α flux of 2×10^{-16} ergs s $^{-1}$ cm $^{-2}$, in agreement with the corrected count predictions of Geach et al. (2010). H α -emitting galaxies with comparable [OIII] flux are roughly five times less common at these ($\sim 1\text{--}3 \times 10^{-16}$ ergs s $^{-1}$ cm $^{-2}$) emission line fluxes.

As emission line fluxes become fainter the H α /[OIII] ratio becomes smaller, largely a result of the correlation between the H α /[OIII] ratio and H α luminosity previously reported by WISP (Domínguez et al. 2013). While great numbers of H α /[OIII] < 1 emission line galaxies can be found around 5×10^{-17} ergs s $^{-1}$ cm $^{-2}$, there are effectively none in our sample once the H α flux becomes greater than 2×10^{-16} ergs s $^{-1}$ cm $^{-2}$. These large H α /[OIII] ratios for the brighter emission lines suggest that 60-80% of the H α emission lines found by future space missions will be single lines. However, that same high H α /[OIII] ratio suggests that the likelihood of contamination by lines besides H α remains low.

Our H α luminosity function found a slightly higher number density of faint line emitters than the NICMOS near-infrared grism surveys, likely a result of the smaller equivalent widths to which the WISP survey is sensitive. We also find our $0.9 < z < 1.5$ number counts to be a bit higher ($1.3\text{--}2\times$) than the $z=1.47$ narrow band H α survey of HiZELS (Sobral et al. 2012), which can not be explained by their minor difference in equivalent width cut-offs. On the other hand, our lower redshift $0.3 < z < 0.9$ H α -emitter number counts are in solid agreement with the narrow band counts from HiZELS at $z=0.84$. However, the lower median redshift of the $0.3 < z < 0.9$ WISP sample suggests that we should find slightly fewer galaxies than HiZELS for the lower redshift sample as well. Taken together, these luminosity function differences suggest that narrow band surveys may be missing some galaxies, although the differences are small enough that the count differences could also be consistent with a $2\text{--}3 \sigma$ statistical outlier.

The [OIII] emission line probes a higher redshift range than H α and is therefore not sensitive to the fainter luminosities required to properly constrain α . If we fix $\alpha = -1.5$, as seen in studies at lower redshifts, we find that the evolution in the [OIII] luminosity function from $z=0.7\text{--}2.3$ is almost entirely in the L_* parameter, which steadily increases with redshift over the sampled range.

We would like to acknowledge the assistance of Chun Ly for his helpful advice during the production of this paper. The authors would also like to acknowledge fi-

nancial support from the grants for HST programs GO-10226, GO-11696, and GO-12283.

REFERENCES

- Atek, H., Siana, B., Scarlata, C., et al. 2011, *ApJ*, 743, 121
- Atek, H., Malkan, M., McCarthy, P., et al. 2010, *ApJ*, 723, 104
- Brammer, G. B., van Dokkum, P. G., Franx, M., et al. 2012, *ApJS*, 200, 13
- Cole, S., Percival, W. J., Peacock, J. A., et al. 2005, *MNRAS*, 362, 505
- Dressler, A., Spergel, D., Mountain, M., et al. 2012, *arXiv:1210.7809*
- Domínguez, A., Siana, B., Henry, A. L., et al. 2013, *ApJ*, 763, 145
- Eisenstein, D. J., & Hu, W. 1998, *ApJ*, 496, 605
- Eisenstein, D. J., Zehavi, I., Hogg, D. W., et al. 2005, *ApJ*, 633, 560
- Felten, J. E. 1977, *AJ*, 82, 861
- Gallego, J., Zamorano, J., Aragon-Salamanca, A., & Rego, M. 1995, *ApJ*, 455, L1
- Geach, J. E., Cimatti, A., Percival, W., et al. 2010, *MNRAS*, 402, 1330
- Geach, J. E., Smail, I., Best, P. N., et al. 2008, *MNRAS*, 388, 1473
- Green, J., Schechter, P., Baltay, C., et al. 2012, *arXiv:1208.4012*
- Henry, A. L., Martin, C. L., Dressler, A., Sawicki, M., & McCarthy, P. 2012, *ApJ*, 744, 149
- Hu, E. M., Cowie, L. L., Kakazu, Y., & Barger, A. J. 2009, *ApJ*, 698, 2014
- Kimble, R. A., MacKenty, J. W., O’Connell, R. W., & Townsend, J. A. 2008, *Proc. SPIE*, 7010
- Kobulnicky, H. A., & Kewley, L. J. 2004, *ApJ*, 617, 240
- Kümmel, M., Walsh, J. R., Pirzkal, N., Kuntschner, H., & Pasquali, A. 2009, *PASP*, 121, 59
- Kümmel, M., Kuntschner, H., & Walsh, J. 2007, *Space Telescope European Coordinating Facility Newsletter*, 43, 8
- Laureijs, R., Gondoin, P., Duvet, L., et al. 2012, *Proc. SPIE*, 8442
- Laureijs, R., Amiaux, J., Arduini, S., et al. 2011, *arXiv:1110.3193*
- Lee, J. C., Ly, C., Spitler, L., et al. 2012, *PASP*, 124, 782
- Lee, J. C., Kennicutt, R. C., Funes, S. J., José G., Sakai, S., & Akiyama, S. 2007, *ApJ*, 671, L113
- Liang, Y. C., Yin, S. Y., Hammer, F., et al. 2006, *ApJ*, 652, 257
- Ly, C., Malkan, M. A., Kashikawa, N., et al. 2007, *ApJ*, 657, 738
- MacKenty, J. W., Kimble, R. A., O’Connell, R. W., & Townsend, J. A. 2010, *Proc. SPIE*, 7731
- Magnelli, B., Elbaz, D., Chary, R. R., et al. 2011, *A&A*, 528, A35
- Martin, C. L., Sawicki, M., Dressler, A., & McCarthy, P. 2008, *ApJ*, 679, 942
- McCarthy, P. J., Yan, L., Freudling, W., et al. 1999, *ApJ*, 520, 548
- McLure, R. J., Jarvis, M. J., Targett, T. A., Dunlop, J. S., & Best, P. N. 2006, *MNRAS*, 368, 1395
- Osterman, S., Green, J., Froning, C., et al. 2011, *Ap&SS*, 335, 257
- Pérez-González, P. G., Rieke, G. H., Villar, V., et al. 2008, *ApJ*, 675, 234
- Pirzkal, N., Rothberg, B., Ly, C., et al. 2012, *arXiv:1208.5535*
- Shim, H., Colbert, J., Teplitz, H., et al. 2009, *ApJ*, 696, 785
- Sobral, D., Smail, I., Best, P. N., et al. 2012, *arXiv:1202.3436*
- Sobral, D., Best, P. N., Geach, J. E., et al. 2009, *MNRAS*, 398, 75
- Thompson, R. I., & Schneider, G. 1998, *Proc. SPIE*, 3356, 215
- Tremonti, C. A., Heckman, T. M., Kauffmann, G., et al. 2004, *ApJ*, 613, 898
- Trenti, M., & Stiavelli, M. 2008, *ApJ*, 676, 767
- van der Wel, A., Straughn, A. N., Rix, H.-W., et al. 2011, *ApJ*, 742, 111
- van Dokkum, P. G., Whitaker, K. E., Brammer, G., et al. 2010, *ApJ*, 709, 1018
- Wang, Y., Percival, W., Cimatti, A., et al. 2010, *MNRAS*, 409, 737
- Weinberg D. H., Mortonson, M. J., Eisenstein D. J., Hirata C., Reiss A. G., Rozo E., 2012, *Phys. Rep.*, submitted (*arXiv:1201.2434*)
- Weiner, B. J. 2012, *arXiv:1209.1405*
- Woodgate, B. E., Kimble, R. A., Bowers, C. W., et al. 1998, *PASP*, 110, 1183
- Yan, L., McCarthy, P. J., Freudling, W., et al. 1999, *ApJ*, 519, L47